Philosophical Magazine
Publication details, including instructions for authors and subscription information:
http://www.tandfonline.com/loi/tphm20

Phase transitions and cyclic pseudotachylyte formation in simulated faults

Yixiang Gan [a], Pierre Rognon [a] & Itai Einav [a]
[a] Particles and Grains Laboratory, School of Civil Engineering, The University of Sydney, 2006 NSW, Australia

Version of record first published: 02 Apr 2012.

To cite this article: Yixiang Gan, Pierre Rognon & Itai Einav (2012): Phase transitions and cyclic pseudotachylyte formation in simulated faults, Philosophical Magazine, 92:28-30, 3405-3417

To link to this article: http://dx.doi.org/10.1080/14786435.2012.669062

Philosophical Magazine
Vol. 92, Nos. 28–30, 1–21 October 2012, 3405–3417

Taylor & Francis
Taylor & Francis Group

Phase transitions and cyclic pseudotachylyte formation in simulated faults

Yixiang Gan, Pierre Rognon and Itai Einav*

Particles and Grains Laboratory, School of Civil Engineering, The University of Sydney, 2006 NSW, Australia

(*Received 4 November 2011; final version received 12 February 2012*)

Field evidence from faults containing pseudotachylytes has revealed cyclical episodes of frictional melting, ductile deformation, and overprinting at a later stage by a new generation of pseudotachylytes. Here we connect these cycles to earthquake dynamics using a development of a discrete element model with solid grains that can melt during frictional heating and viscous melts that can bond through solidification during cooling. A new earthquake episode initiates with the crushing of bonded clusters once the bond strength is exceeded, with frictional shear heating being activated again. We explore the competition between melting and solidification in terms of phase transitions using scaling laws dependent on the characteristic times for melting, thermal diffusion and loading rates. A phase diagram is constructed that is capable of explaining the tendencies towards pseudotachylytes associated to cataclasites or mylonites, depending on the fault conditions (its depth and thickness, crust motion and ambient temperature) and the mechanical and thermal parameters defining the grains within the fault and the host rock.

Keywords: fault dynamics; pseudotachylytes; discrete element method; phase transitions; melting; shear localization

1. Introduction

The production of melts within localized shear zones during faulting can become critical for fault dynamics [1–6]. Once formed, melts can act either as a coseismic fault lubricant [7,8] or as a viscous brake to the earthquakes [9]. Faults present rheology that strongly varies with depth [10]. In that respect, faults with evidence of melted material in the form of pseudotachylytes may be a reliable indicator for ancient seismic activities in exhumed faults [11–14]. Various studies of frictional instability and thermal runaway have been based on a macroscopic energy balance between heat production in the slipping zone and heat diffusion across fault wall rocks [15,16], and Veveakis *et al.* [17] discussed the significance of the Gruntfest number in their analysis of thermal runaway during landslides. Veveakis *et al.* [18] demonstrated that the Arrhenius temperature dependence of the friction law does not favor the prediction of thermal runaway in sheared faults.

*Corresponding author. Email: itai.einav@sydney.edu.au

ISSN 1478–6435 print/ISSN 1478–6443 online

http://dx.doi.org/10.1080/14786435.2012.669062
http://www.tandfonline.com

Exhumed pseudotachylytes from Central Australia have revealed cyclical episodes of frictional melting, ductile deformation, overprinted at a later stage by a new generation of pseudotachylytes [19]. Two types of pseudotachylyte rocks have been distinguished, including pseudotachylytes associated to cataclasites [20] and mylonites [19]. Pseudotachylytes associated to cataclasites support the model of Sibson [11], which describes the transition from elasto-frictional solids to viscous-plastic shear zones. The presence of mylonite-associated pseudotachylytes favors an alternative model, first proposed by Hobbs *et al*. [19], which describes the nucleation of ductile instabilities that allow the transition from unstable to stable flow in crustal rocks. An alternative model to interpret the association of pseudotachylytes with mylonites is downward propagation of seismic ruptures in the lower crust [21]. Here we develop a micromechanical approach to construct a general phase diagram dependent on the characteristic times for melting, thermal diffusion, and loading rates, at this stage without accounting for crystal-plastic deformations that possibly dominate in deeper faults [22].

The development of melt within the faults can be associated with critical weakening factors. Such factors have been studied at the scale of laboratory tests. Spray [23] showed in experiments performed on solid granite that grain comminution is a precursor to friction melting. Through experiments with solidification of melted asperity contacts prior to bulk melting, Tsutsumi and Shimamoto [24] proposed that the initial peak in friction was due to welding of the asperities. Recently, Di Toro *et al*. [8] carried out experiments on solid rocks to measure rock friction in the presence of melts under seismic slip conditions. Using theoretical studies with the consideration of the rate and state friction law, fault weakening was associated with either flash heating involving localized asperity melts [5], or global melting [18,25]. Finally, numerical models using the discrete element method (DEM) have been used to study fault localizations with a focus given to comminution [26,27], stick-slip driven by local force chain buckling between the grains [28], and the thermal convection arising from the dispersed granular motions and temperatures within the fault [29]. The method of Rognon and Einav [29] is specifically relevant to the current paper, in that it accounts for heat transfer between grains. However, this work did not consider aspects of heat generation and subsequent melting processes, which are critical to pseudotachylyte rocks. Here this method is extended with added details accounting for the melting of the grain surfaces, melt viscosity, solidification of melts, and deboning of the solidified melts. In this Meltable-DEM model, heat generation comes from intergranular viscous damping and most importantly from intergranular friction.

2. Dimensionless numbers

We start by identifying the key parameters for an idealized fault model accounting for thermal diffusion and mechanical stick-slip dynamics. The fault under consideration is located at a depth H, with a fault core thickness h, as shown in Figure 1a. The mechanical boundary to the fault layer is imposed via a spring–dashpot system with a spring stiffness K_D and a damping factor η_D. The spring stiffness K_D is here taken as $K_D = G/H$, with G being the shear modulus of the rock. A constant dragging

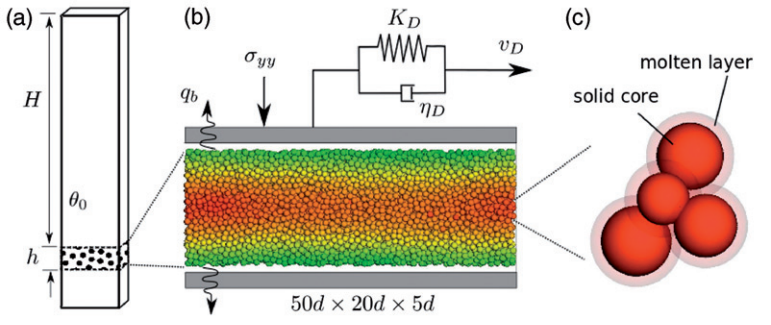

Figure 1. Model schematics: (a) rock mass with a fault located at depth H, with thickness h, and ambient temperature θ_0; (b) boundary conditions for the Meltable-DEM with the spring–dashpot system representing the intact rock above the fault, d denoting the average grain diameter, σ_{yy} being the effective vertical stress, q_b denoting the heat flux diffused to the environment and K_D, η_D and v_D referring to the Earth's crust parameters including the effective shear stiffness, the damping dashpot constant and the dragging velocity, respectively; (c) grains with molten layers.

velocity of the mass center of the intact rock, v_D, is assumed to capture the stick-slip response as a model feedback (i.e., here the stick-slip develops naturally due to micro-thermomechanical processes at the particle scale). The shear stress inside the fault core builds up by the continuous movement of the intact rock. As the shear stress increases above a certain shear stress threshold τ_p, a slip event initiates, and the elastic energy stored within the surrounding rock releases (captured by the rebound of the spring K_D). As a result, the localized shear deformation within the fault introduces frictional dissipation, which rapidly elevates the fault core temperature. On the other hand, this tendency towards higher temperatures is balanced by the heat exchange between the fault and the surrounding, defined via $q_b = k_s(\theta - \theta_0)/h$, with q_b, k_s, θ, and θ_0, being the surface heat flux directed outwards, the thermal conductivity of the rock, the average fault temperature and the ambient temperature, respectively.

The fault material is characterized by grains with an average diameter d, where $d \ll h$. The material parameters of the grains include: ρ = density; k_s = thermal conductivity; c_p = heat capacity; and $\Delta\theta_m = \theta_m - \theta_0$ with θ_m being the melting temperature. Natural faults may involve several minerals with a variety of such parameters [30]. For simplicity, our current fault model involves only a single set of such parameters, which may reflect an approximated volume average of the distinct mineral species. To describe such a stick-slip system we choose two dimensionless numbers, describing the system diffusivity $\mathcal{G}$, similar to the Gruntfest number [31], and the fault meltability $\mathcal{M}$, as:

$$\mathcal{G} = \frac{t_c}{t_m} = \frac{\rho g H v_D h}{k_s \Delta\theta_m}, \quad \mathcal{M} = \frac{t_{\dot{\gamma}}}{t_m} = \frac{gH}{c_p \Delta\theta_m}. \tag{1}$$

Our Gruntfest number, $\mathcal{G}$, compares the time for heat to diffuse to the environment (cooling time $t_c = \rho c_p h^2/k_s$) with the time taken for the system to increase its core

temperature towards the melting point (melting time $t_m = c_p \Delta\theta_m h/(gHv_D)$, with $g = 9.8$ m/s^2). The melting time reflects a simple energy balance between work input $\tau_p v_D t_m$ and the storage of heat $\rho c_p \Delta\theta_m$. The shear stress threshold τ_p may be assumed to scale with the lithospheric stress $\sigma_{yy} \approx \rho g H$, since peak friction coefficients tend to be close to unity [32]. Our meltability number, $\mathcal{M}$, compares the shear time $t_{\dot\gamma} = \dot\gamma^{-1} = h/v_D$ with the melting time t_m. Table 1 presents a compilation of the required parameters from representative pseudotachylytes. Using the values in Table 1, Table 2 presents the dimensionless numbers corresponding both to the geological and simulation scales. Most importantly, the characteristic times in the simulations have been selected to ensure preservation of the same order of $\mathcal{G}$ and $\mathcal{M}$.

3. Meltable discrete element method

3.1. *Method summary*

Conventional DEM describes the motion of grains using Newton's law of motion, while their interaction is represented using mechanical contact laws [35]. An extension of this method was proposed by Vargas and McCarthy [36] which enables

Table 1. Typical parameters used in the literature.

Ref.	H (km)	θ_0 (°C)	θ_m (°C)	ρ (kg/m)^3	c_p (J/kg°C)	k_s (W/m°C)	h (mm)
[1]	4–5	$\Delta\theta_m = \theta_m - \theta_0 \approx 800$		2800	1020[a]	2	10
[2]	3	110–160	750–1280	2500	–	–	2–20
[30][b]	9–11	250–300	657–1726	2600–2709	1090–1186	1–7	6–24
[13]	1.6–7	–	–	–	–	–	1–390
[25]	7	210	1000	2700	1000	1.89	5–10
[14]	–	$\Delta\theta_m > 1200$		2850	1150	4.92[c]	20–380
[33][d]	1.6–7	–	750–1400	–	–	–	–
Geological scale[e]	[1,11]	$\Delta\theta_m \in [357,1500]$		[2500,2850]	[1000,1186]	[1,7]	[1,390]

Notes: [a]c_p is evaluated from Sibson [1], using $c_p = k_s/(\kappa\rho)$ where κ is the thermal diffusivity given in the reference.
[b]Values represent all the minerals mentioned by Di Toro and Pennacchioni [30] with a solid fraction above 1%.
[c]k_s is evaluated from Andersen and Austrheim [14], assuming $k_s = \kappa\rho c_p$.
[d]Values from Lin [33] were compiled from multiple sources, as presented in his Table 8.7.
[e]In addition, the dragging velocity was estimated by the bound given for slow deformation [34], $v_D \in (0, 10^{-3}]$ m/s.

Table 2. Time-scales and dimensionless numbers used in this study.

	$t_{\dot\gamma}$	t_c	t_m	$\mathcal{G}$	$\mathcal{M}$
Geological scale	$[1, \infty]$	$[0.36, 5.1 \times 10^5]$	$[3.3, \infty]$	$[0, 3.4 \times 10^2]$	$[5.5 \times 10^{-3}, 0.30]$
Simulation scale	10^2	$[10^{-1}, 10^3]$	$[10^2, 10^4]$	$[10^{-3}, 10^2]$	$[10^{-2}, 10^0]$

the transfer of heat along grain contacts by a simple Fourier law of conduction, and has already been applied successfully to the problem of fault shear [29]. We extend this method to develop Meltable-DEM, starting by adding the heat generation from friction and viscous mechanical dissipation effects. We capture transitions from solid to melt and vice versa by partitioning the grains into separate molten and solid phases; the geometries and time evolution of these distinct phases are simplified to describe a spherical solid core and a shell-like flash-melt-layer. Contact dynamics between meltable grains are considered by adding the contribution of melt viscosity to the overall mechanical interaction. Melting or solidification of isolated grains evolves either by increasing or reducing the shell thickness Δ, respectively. Solidification can further develop a bond between two grains if they have melt-layers in contact, which results in clustering; such bond clusters can degrade either through de-bonding or re-melting.

3.2. *Details of the method*

For a single grain, the evolution of the molten layer thickness Δ can be obtained by considering the amount of latent heat, the continuous supply of heat transfer from the contacting grains, and the heat generation through the grain contacts:

$$\dot{\Delta}(t) = \frac{\dot{\phi}}{4\pi R_s^2(t)\rho L_{\mathrm{m}}}, \quad \text{if } \theta \geq \theta_{\mathrm{m}}, \tag{2}$$

where R_s is the radius of the solid core; $\dot{\phi}$ is the rate of change of the heat including the rates of heat transfer through contacts calculated according to [36], and adding heat generation calculated using the intergranular mechanical dissipation; ρ and L_{m} are the density of the material and the latent heat, respectively. The latent heat was estimated using $L_{\mathrm{m}} \propto c_p \Delta\theta_{\mathrm{m}}$, consistent with data from [30].

Figure 2 shows one example of the contact dynamics between two grains, including melt-layers. In the most general case the contact area between two meltable grains can be divided into three regions: a molten contact region represented by viscous interaction, a solid contact region by a Hertzian contact, and a bonded region. The typical models of the normal interaction for different stages of an intergrain contact are shown in Figure 2a–c; we emphasize that the crossovers between these stages are continuous. Compared to the conventional Hertzian contact force, the normal elastic force between the i-th and j-th grains is calculated based on the effective solid radius R_s^* and the solid overlap $\delta_s = \delta - \Delta_i - \Delta_j$ as

$$\mathbf{F}_n^{\mathrm{ela}} = \begin{cases} -E^*(a_s\delta_s - a_b\delta_b)\mathbf{n} & \delta_s > \delta_b \\ -\dfrac{3}{2}E^* a_b(\delta_s - \delta_b)\mathbf{n} & \delta_s \leq \delta_b. \end{cases} \tag{3}$$

Here, a_s, a_b and δ_b are the solid contact radius, bonding radius and bonding overlap, respectively. The above equation guarantees the continuity of both the elastic force F_n^{ela} and its derivative with respect to solid deformation through $\partial F_n^{\mathrm{ela}}/\partial\delta_s$ at the transition between compression and tension. From the classical Hertzian solution,

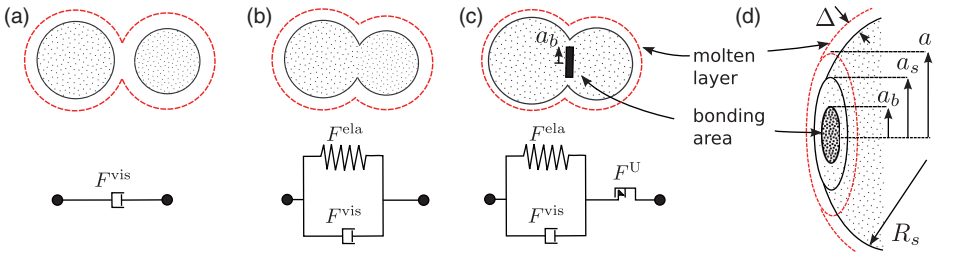

Figure 2. Contact interaction between two meltable grains: (a) contact between two molten layers, including the viscous force $F^{vis} = \eta v$, where η and v are the damping factor and relative velocity, respectively; (b) contacts with interacting solid cores, including the elastic force F^{ela} using the Hertzian law and F^{vis}; (c) formation of bonds by a solidification process, with the bond radius a_b, including the ultimate bonding force $F^{U} = \pi a_b^2 \sigma^{U}$, modification of the Hertzian law to include the bonding effect F^{ela}, and F^{vis}, where σ^{U} is the material strength; (d) 3D representation of the last scenario, where Δ, R_s, a and a_s denote the thickness of the melt-layer, the radius of the solid core, the overall contact radius, and the solid contact radius, respectively.

the effective elastic modulus is expressed as

$$E^* = \frac{4}{3}\left[\frac{1-\nu_i^2}{E_i} - \frac{1-\nu_j^2}{E_j}\right]^{-1}. \tag{4}$$

The heat transfer through the contact is calculated based on the total contact radius $a = \sqrt{R^*\delta}$ accounting for all three contact regions shown in Figure 2d, where R^* is the effective radius. The heat flux between the i-th and j-th grains can thus be defined by $\phi_{ij} = -2ak_s(\theta_j - \theta_i)$ [36,37]. We use the same conductivity for both solid and molten phases, in order to consider the lower bound of the cooling time since melts are known to have reduced conductivity [30]. The intergrain friction coefficient used in this study is set to $\mu = 0.5$. Along contacts involving melts the friction coefficient is removed due to the lubrication effect of the melted compositions [8,38]. Viscous damping then provides an alternative but significantly reduced heat generation source, associated with a marked transition from friction-dominated to viscous-dominated flows. Also, melt viscosity at the contact-level is assumed constant with temperature, $\eta \approx 1$ Pa.s, while we also ignore possible viscous-lubrication effects from squeezing of melt due to high contact forces. On the other hand, at macroscopic fault-level the increase in melt volume by our model may consistently explain the decrease in macroscopic viscosity with fault-average temperatures observed in [1,2,14].

In our method, solidification in the form of bonding develops when the sum of the melt thicknesses of two contacting grains reduces, i.e., $\dot{\Delta}_i + \dot{\Delta}_j < 0$ (as expected during cooling). After such a bond has been created, the bonding area can either shrink via melt growth or further grow via additional cooling. Assuming the bond area initiates from the center of the solid contact region during the solidification process, the radius of the bond a_b between the contacting i-th and j-th grains can be calculated by:

$$a_b = \sqrt{R_s^* \delta_b}, \quad \text{where } \delta_b = -\int_t (\dot{\Delta}_i + \dot{\Delta}_j) H(\delta_s) \mathrm{d}t, \tag{5}$$

where δ_b is the solid overlap portion attributed to the bond, ranging from 0 to δ_s. The second part of the equation derives from the compatibility between solidification and bonding processes at the interface level; for that purpose we have introduced the unit step function $H(\delta_s)$, i.e., enabling a change to δ_b only when the solid contact is present. The resulting solid bond can sustain tensile and tangential forces (F_n and F_t), and rolling and twisting moments (M_r and M_w), up to rupture defined by a Mohr–Coulomb type of failure criterion accounting for all of these four loading modes. The bond failure criterion depends on a single strength threshold parameter, σ^{U}. The system was found to be only weakly sensitive to this parameter for all values between 0.2% and 2% of the bulk Young's modulus.

4. Simulated faults

4.1. *Typical stick-slip cycle during the DEM simulations*

A three-dimensional representative volume element containing 5,000 or 10,000 grains has been subjected to loading as shown in Figure 1b. Stick-slip is then observed to occur naturally during our simulations with consideration of melting. Consistent with Spray [23], slip initiates through comminution of clustered "super-particles" (here formed during the previous stick process involving melt-solidification). As a result of the thermomechanical contact rheology, those super-particles are left to develop individual geometries, each having a unique agglomerated shape comprising any possible number of spherical units. The boundaries are fully periodic for grain motion; for grain temperatures they are periodic only about the four orthogonal faces to the fault plane, while on the other two faces heat flux is controlled by q_b. The damping factor η_{D} is set to be sufficiently small to simulate the fraction of energy radiated by earthquake waves when the shear rate is significantly high, and this mechanism only serves for stabilizing the solution during high slip velocities. A long simulation time is required to capture the cyclic behavior over time. Since the time interval between natural earthquakes is rather long, for the simulations material parameters have been chosen to reduce the computational time implied from the geological parameters listed in Table 1. As demonstrated in Table 2 this was achieved by selecting smaller values of c_p and $\Delta\theta_{\mathrm{m}}$ and larger values of v_{D} to get shorter $t_{\dot{\gamma}}$, without altering the order of magnitude of the dimensionless numbers $\mathcal{G}$ and $\mathcal{M}$.

4.2. *System behavior and cyclic melting*

The results from 24 simulations are shown in Figure 3a, with a symbol categorizing whether they belong to different observed phase regimes. In Figure 3b, three typical evolutions of shear stress and the average fault temperature are plotted over time. Each of these three simulations belongs to a different phase regime, with responses that are clearly distinguishable. Those three phases denote: (i) a fully melting regime, where the grains are not able to cool down and solidify between two consequent slip events; (ii) a cyclic melting regime, where the average temperature is rising sufficiently to cause grain melting during slip, but the system can sufficiently cool down between the slips to form new intergranular bonds; and (iii) a non-melting regime, with a typical low-amplitude stick-slip behavior without any grain reaching

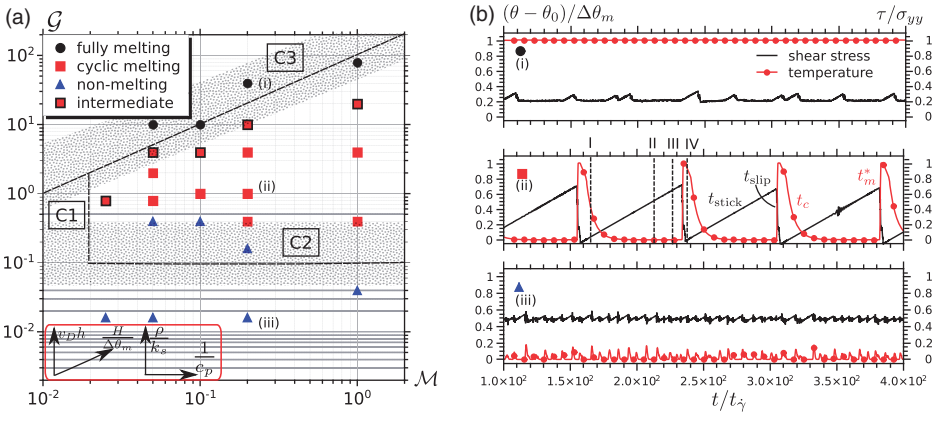

Figure 3. (a) Phase diagram of cyclic melting in faults plotted using two dimensionless numbers, $\mathcal{M}$ and $\mathcal{G}$. Data points show results from a range of Meltable-DEM simulations, with symbols referring to various types of observed system responses. Dashed lines are the three conditions, Equations (6)–(8), resulting from scaling considerations. Shaded areas designate one order deviation from the ideal scaling laws. Arrows show the system dependence on the various material and environmental parameters. (b) Time evolutions (t) of the normalized average fault core temperature, $(\theta-\theta_0)/\Delta\theta_{\rm m}$, and shear stresses, τ/σ_{yy}, from three typical simulations, corresponding to points (i) fully melting regime, (ii) cyclic melting regime and (iii) non-melting regime of the left phase diagram.

the melting point, and therefore without introducing any form of solidification. Furthermore, these three phase regimes reveal totally distinguishable modes of motion: (i) the fully melting regime involves viscous dominated motion; (ii) the cyclic melting regime develops high-magnitude stick-slip motions; and (iii) the non-melting regime also with stick-slip motion but with much smaller magnitudes. Given the particulate nature of our simulated fault, all three regimes present intermittent time-dependent variation in the shear stress, which are mostly neglected from deterministic predictions using previous continuum models. Most interestingly, in the cyclic melting regime, the average fault temperature during the slips (i.e., over time denoted in the figure as $t_{\rm slip}$) rapidly reaches the melting temperature (i.e., mostly over a shorter time denoted in the figure as $t_{\rm m}^*$). In return, a stick phase develops over a time $t_{\rm stick}$, associated with the rise of the shear stress, which is mostly longer than the thermal diffusion time, $t_{\rm c}$. Five simulations present intermediate dynamics, and are marked specially in the phase diagram. In those cases $t_{\rm c} \geq t_{\rm stick}$, i.e., solidification evolves after slip but with the cooling time not sufficiently long to reduce the average fault temperature towards the ambient temperature before the next slip event.

The time is normalized by the simulation shear time in Figure 3b, as $t/t_{\dot\gamma}$. The normalized time interval observed between two simulated slip events in the cyclic melting regime is in the range of $\Delta t/t_{\dot\gamma} = \Delta t v_{\rm D}/h \approx 100$. This can be mapped to geological time interval by selecting appropriate parameters. For example, assuming geological crust motion of $v_{\rm D} = 10$ cm/year and fault core thickness $h = 1$ cm, our simple model predicts the geological time interval between two earthquakes to be of the order of $\Delta t \approx 10$ years. It is important to note that our model refers only to a single active fault independent of non-local interactions with other nearby faults,

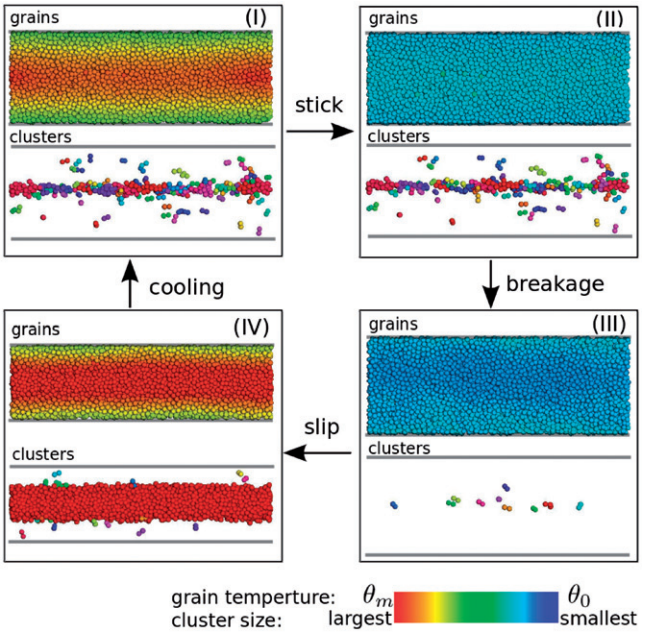

Figure 4. Stages from a typical Meltable-DEM simulation belonging to the cyclic melting regime, shown in Figure 3b. For each stage from I to IV, the upper subfigure shows all grains colored by their temperatures, and the lower subfigure shows only clusters colored by the number of bonded grains they contain.

which represents an underestimation factor to the predicted time interval. The periodicity of our simulation cell implies simultaneous slip along the entire fault, which introduces an overestimation factor to the predicted time interval Δt. Together, these two competing factors may compensate each other, thus possibly supporting our model prediction. Also, it is important to note that the prediction of the local fault model of the near-periodic behavior in regime (ii) does not exclude aperiodicity at the much larger geophysical scale, which is controlled by the full rock network beyond our model view.

Figure 4 shows the four typical stages corresponding to simulation case (ii) in Figure 3b, i.e., in the cyclic melting regime. Each stage is represented by two subfigures. The first subfigure shows all grains within the fault with color denoting their temperatures. The second subfigure shows only those grains belonging to super-particles. A single super-particle includes the agglomerate of all unit spheres interconnected via solidified bonds; this super-particle is distinguished from the others in Figure 4 using a color dependent on the number of spherical units it contains. These four typical stages are repeatedly found during the simulated earthquakes in the cyclic melting regime, and represent: (I) a cooling stage subsequent to a slip event; (II) a stick stage where the overall shear stress increases gradually, but without much topological change to the super-particles; (III) a comminution stage at higher shear stresses that includes the rapid breakage of the super-particles; and (IV) a slip stage where the amount of energy released raises

temperatures towards the melting temperature, followed by a cooling stage already described as stage (I).

In the cyclic melting regime, just after slip initiation, only a few local melts are being created at the contact level. Such localized melts have two major effects, first they locally remove frictional heat generation and second they reduce the overall shear resistance. This gradually escalates the shear instability due to the growing disparity between the shear stress in the rock-spring K_D (which was built-up during the previous stick phase) to the *in situ* fault shear resistance (which reduces due to the creation of the melt). Consequently, the fault temperature reaches global melting, and thus the shear stress drops with dramatically larger energy release compared to the non-melting regime scenarios. This is consistent with the thermal runaway problem in experimental and theoretical investigations [16,18].

5. Phase diagram

Next, we develop scaling laws that are capable of explaining the observed behavioral differences in Figure 3. Such laws are formulated to detect the conditions to be in the cyclic melting regime (b), by comparing the four characteristic time-scales, t_{stick}, t_{slip}, t_c and t_m^*, as shown in Figure 3.

5.1. *Thermomechanical conditions*

C1 – Slip time longer than melting time

Assuming that the shear stress resistance after melting is much lower than τ_p, and that the shear stress decreases linearly with the slip, the condition to stay in the cyclic melting regime (b) can be formulated to guarantee that the dissipative mechanical energy produced during a single slip event would be sufficiently large to reach the melting point of the fault. This is achieved by requiring the slip time to be greater than or equal to the melting time, $t_{slip} \geq t_m^*$. The slip time could be evaluated as $t_{slip} = D/(2v^*)$, while the melting time is $t_m^* = c_p \Delta\theta_m h/(gHv^*)$. Here, the melting time t_m^* is local and is thus taken according to the slip velocity v^*, and not due to the dragging velocity v_D defining the global melting time t_m. Also, D represents the total slip distance for the full shear stress drop, which is related to the reduction of the stress in the cyclic melting regime as $D \sim \tau_p/K_D$. Condition C1 can therefore be expressed in terms of the meltability number discussed before:

$$\mathcal{M} \geq 2\frac{h}{D}, \tag{6}$$

which is independent of the Gruntfest number $\mathcal{G}$.

C2 – Cooling time longer than melting time

While the previous condition required that the heat generation would be sufficient for melting, such melting can only be achieved if the amount of heat escaping from the fault during the slip is not dominating. For that purpose, the cooling time is required to be longer than or equal to the melting time, as $t_c \geq t_m^*$, guaranteeing that

such faults stay in the cyclic melting regime (b). In other words, melting can only develop if the heat diffusion rate is smaller than the heat production rate in the slipping zone. Condition C2 can therefore be expressed in terms of the Gruntfest number discussed before:

$$\mathcal{G} \geq \frac{v_{\mathrm{D}}}{v^*}, \tag{7}$$

which is independent of the meltability number $\mathcal{M}$. Also notice that the slip velocity v^* is not known a priori, but in any case is much faster than the dragging velocity, as $v^* \gg v_{\mathrm{D}}$. Notice that Equation (7) does not appear to be a simple form with $\mathcal{G} \geq 1$ as $t_{\mathrm{c}} \geq t_{\mathrm{m}}$, since we are replacing the overall melting time t_{m} with the local counterpart t_{m}^*. The local melting time represents the actual characteristic time of the slip. In natural faults, proximity to condition C2 can be connected with pseudotachylytes associated to cataclasites, since such transitions occur between brittle and ductile behaviors. It is important to note that our model does not introduce possible aspects of recrystallization, which may exclude pseudotachylyte formations where cooling occurs very rapidly.

C3 – Stick time longer than cooling time

Irrespective of the previous conditions dealing with the melting time, staying in the cyclic melting regime (b) requires that between two consecutive slip events the fault could cool down back to its ambient temperature. For that to happen the stick time t_{stick} is required to be longer than or equal to the cooling time, as $t_{\mathrm{stick}} \geq t_{\mathrm{c}}$. The stick time can be evaluated by equating the elastic stress and the peak stress, given as $t_{\mathrm{stick}} = \tau_p/(K_{\mathrm{D}} v_{\mathrm{D}})$. Condition C3 can therefore be expressed in terms of both dimensionless numbers as:

$$\frac{\mathcal{M}}{\mathcal{G}} \geq \frac{h}{D}. \tag{8}$$

In natural faults, proximity to condition C3 can be related to pseudotachylytes associated with mylonites, which marks the transition between unstable flows to stable ductile rocks.

These inequalities, as in Equations (6)–(8), are plotted in Figure 3 with the data points from the simulations mentioned before. The predicted theoretical conditions define a complete phase diagram that is consistent with the results provided by the Meltable-DEM simulations. The lines shown correspond not only to the actual parameters used for the simulations, but also to their equivalent natural earthquake parameters, defined by $K_{\mathrm{D}} \approx 10^8$ Pa/m, $\tau_p \approx 10^8$ Pa, $h \approx 10^{-2}$ m and $v^*/v_{\mathrm{D}} \approx 10$.

6. Conclusion

In this paper a meltable discrete element method (Meltable-DEM) has been proposed that extends previous DEM models including thermal diffusion between grain contacts. Important features of our proposed Meltable-DEM are details provided on how to include grain melting, melt solidification, bonds creation and

breakage. The Meltable-DEM was then adopted to explore pseudotachylyte formation and cyclic melting of faults. The study involved a series of simulations that were represented by two dimensionless numbers (Gruntfest and meltability). The mark transitions between various observed fault responses and formations have been identified, and understood by comparing the theoretical characteristic times requiring to stay in the so-called cyclic melting regime. This regime is extremely relevant to earthquake studies, as it targets a fundamental stick-slip process that involves the melt-solidification phase changes of grains. The theoretical dimensionless analysis provided three conditions that agreed nicely with the observed simulations by the Meltable-DEM model.

Our phase diagram is capable of explaining transitions dependent on environmental and thermomechanical parameters. The way the system depends on these parameters is represented by the arrows embedded in the phase diagram Figure 3a. According to Equation (7), transition from the non-melting to cyclic melt regimes can arise from various sources: (1) deeper faults and higher ambient temperatures, in agreement with [11]; (2) thicker localized shear zone; (3) higher crust velocity; and finally (4) lower material diffusivity.

Future work should acknowledge the level of approximation we had to accept for such a first-order investigation. In particular, our study included the following assumptions: (1) the intact rock moves with a constant average velocity v_D; (2) the simulated fault was isolated from any other fault in the system, and thus the cycles of earthquake reactivations always occurred through the same clustered material; (3) although unit elements agglutinated into amorphous cluster-shape possible, the unit element shape was spherical; (4) inside the fault, there is only one set of material properties, with the same melting point and thermal properties. In future work it may be imperative to allow for realistic unit shapes, with a multitude of mineral compositions, agreeing with actual environmental variables.

Acknowledgments

Financial support for this research from the Australian Research Council, through grant DP1096958, is gratefully appreciated. The authors would like to thank Dr. E. Veveakis for fruitful discussions and the reviewers for their generous and helpful comments.

References

[1] R.H. Sibson, Geophys. J. Royal Astron. Soc. 43 (1975) p.775.
[2] K. Otsuki, N. Monzawa and T. Nagase, J. Geophys. Res. 108 (2003) p.2192.
[3] G. Di Toro and G. Pennacchioni, Tectonophysics 402 (2005) p.55.
[4] Y. Fialko and Y. Khazan, J. Geophys. Res. 110 (2005) p.B12407.
[5] A.W. Rempel and J.R. Rice, J. Geophys. Res. 111 (2006) p.B09314.
[6] T. Putelat, J.R. Willis and J.H.P. Dawes, Phil. Mag. 88 (2008) p.3219.
[7] H. Jeffreys, Geol. Mag. 79 (1942) p.291.
[8] G. Di Toro, T. Hirose, S. Nielsen, G. Pennacchioni and T. Shimamoto, Science 311 (2006) p.647.
[9] Y. Fialko, J. Geophys. Res. 109 (2004) p.B01303.
[10] R.E. Holdsworth, Science 303 (2004) p.181.

[11] R.H. Sibson, J. Geol. Soc. 133 (1977) p.191.
[12] C.H. Scholz, *The Mechanics of Earthquakes and Faulting*, Cambridge University Press, Cambridge, UK, 2002.
[13] J. Allen, Tectonophysics 402 (2005) p.37.
[14] T. Andersen and H. Austrheim, Earth Planet. Sci. Lett. 242 (2006) p.58.
[15] P.B. Kelemen and G. Hirth, Nature 446 (2007) p.787.
[16] T. John, S. Medvedev, L.H. Rüpke, T.B. Andersen, Y.Y. Podladchikov and H.K. Austrheim, Nature Geosci. 2 (2009) p.137.
[17] E. Veveakis, I. Vardoulakis and G. Di Toro, J. Geophys. Res. 112 (2007) p.F03026.
[18] E. Veveakis, S. Alevizos and I. Vardoulakis, J. Mechan. Phys. Solids 58 (2010) p.1175.
[19] B.E. Hobbs, A. Ord and C. Teyssier, Pure Appl. Geophys. 124 (1986) p.309.
[20] J. Magloughlin, Tectonophysics 204 (1992) p.243.
[21] R.H. Sibson, J. Struct. Geol. 2 (1980) p.165.
[22] R.J. Twiss and E.M. Moores, *Structural Geology*, Vol. 22, W. H. Freeman, San Francisco, 2009.
[23] J.G. Spray, Geology 23 (1995) p.1119.
[24] A. Tsutsumi and T. Shimamoto, Geophys. Res. Lett. 24 (1997) p.699.
[25] J.R. Rice, J. Geophys. Res. 111 (2006) p.B05311.
[26] Y. Guo and J.K. Morgan, J. Geophys. Res. 113 (2008) p.B08417.
[27] S. Abe and K. Mair, Geophys. Res. Lett. 36 (2009) p.L23302.
[28] M.P. Ciamarra, E. Lippiello, C. Godano and L. de Arcangelis, Phys. Rev. Lett. 104 (2010), Article No. 238001.
[29] P. Rognon and I. Einav, Phys. Rev. Lett. 105 (2010), Article No. 218301.
[30] G. Di Toro and G. Pennacchioni, J. Struct. Geol. 26 (2004) p.1783.
[31] I.J. Gruntfest, Trans. Soc. Rheol. VII (1963) p.195.
[32] J.D. Byerlee, Pure Appl. Geophys. PAGEOPH 116 (1978) p.615.
[33] A. Lin, *Fossil Earthquakes: The Formation and Preservation of Pseudotachylytes*, Springer, Berlin, 2008.
[34] G.C. Beroza and T.H. Jordan, J. Geophys. Res. 95 (1990) p.2485.
[35] P.A. Cundall and O.D.L. Strack, Géotechnique 29 (1979) p.47.
[36] W.L. Vargas and J.J. McCarthy, AIChE J. 47 (2001) p.1052.
[37] G.K. Batchelar, F.R.S. O'Brien and R.W. O'Brien, Proc. Royal Soc. A: Math. Phys. Eng. Sci. 355 (1977) p.313.
[38] G. Di Toro, D.L. Goldsby and T.E. Tullis, Nature 427 (2004) p.436.